Small-Angle X-Ray Scattering Analysis of Colloidal Crystals and Replica Materials Made From L-Arginine Stabilized Silica Nanoparticles

Pratibha Mahale,[1*] Byeongdu Lee,[2] Hiu Yan Cheng,[3] Mo Segad,[4] and Thomas E. Mallouk[1]

[1]Department of Chemistry, University of Pennsylvania, Philadelphia, PA 19104 USA

[2]Advanced Photon Source, Argonne National Laboratory, Argonne, IL 60439 USA

[3]Department of Chemistry, Pennsylvania State University, University Park, PA 16801 USA

[3]Department of Chemistry, Pennsylvania State University, University Park, PA 16801 USA

[4]Materials Research Institute, Pennsylvania State University, University Park, PA 16801 USA

Abstract: Colloidal crystals made from sub-100 nm silica nanoparticles have provided a versatile platform for the template-assisted synthesis of three-dimensionally interconnected semiconducting, metallic, and magnetic replicas. However, the detailed structure of these materials has not yet been characterized. In this study, we investigated the structures of colloidal crystalline films and germanium replicas by scanning electron microscopy (SEM) and small angle x-ray scattering (SAXS). The structures of colloidal crystals made by evaporative assembly depends on the size of L-arginine-capped silica nanoparticles. Particles smaller than ~31 nm diameter assemble into non-close packed arrangements (bcc) whereas particles larger than 31 nm assemble into random close packed structures with 2D hexatic phase. Polycrystalline films of these materials retain their structure and long-range order upon infiltration at high temperature and pressure and the structure is preserved in Ge replicas. The shear force during deposition and dispersity of silica nanoparticles contributes to the size-based variation in structure and to the size of crystal domains in the colloidal crystal films.

Keywords: silica nanoparticles, assembly, three-dimensional nanostructures, templates, high pressure deposition, small angle X-ray scattering, long range order, L-arginine stabilized silica, evaporative colloidal crystal growth.

Introduction: Colloids are interesting for both fundamental and practical reasons, ranging from their use as model systems of atomic motion in crystals to applications in cosmetics, electronics, optics, catalysis, batteries, diagnostics, and drug delivery.[1–6] A defining characteristic of colloidal systems is the ability to control the size, shape and surface chemistry of the constituent particles. This flexibility has enabled colloidal particles to be used as building blocks for structurally well-defined 2D and 3D assemblies that are periodic over nanometer to micron length scales.[7–12] Colloidal assembly is also a starting point for interconnected replica structures of metals, semiconductors, polymers and inorganic oxides with applications in filtration, sensing, catalysis, optics and electronics.[13–21]

Latex/polystyrene and silica particles have been widely used as building blocks of colloidal crystal and replica structures because of their ease of synthesis, flexible surface chemistry, colloidal stability and ease of template removal post-infiltration. However, in both cases it has been challenging to obtain highly monodisperse particles in the sub-30 nm size range. Stober, *et al.*[22] introduced the ammonia catalyzed hydrolysis of silicon alkoxides in aqueous media in 1968, and this method and its modifications enabled the synthesis of monodisperse silica nanoparticles with diameters greater than 200 nm. A surfactant-assisted microemulsion approach was later developed to make silica colloids in the 30-60 nm size range.[23,24] The use of non-polar organic solvents and large amounts of surfactants, however, limited the microemulsion approach to certain applications. A significant breakthrough by Yokoi, et al.[25] enabled the synthesis of 12-23 nm silica nanoparticles in aqueous media by using amino acids as the catalyst for hydrolysis and condensation of silicon alkoxides. Amino acids stabilized the silica nanoparticles due to their interactions with the surface under basic conditions. Hartlen, *et al*.[26] and Watanabe, *et al*.[27] further developed this approach and optimized it for sizes ranging from 15-200 nm. Their modifications included heterogenous delivery of the silica precursor from an organic layer and separation of the nucleation and growth stages by using a seed-regrowth approach. The as-synthesized silica nanoparticles formed stable colloids due to their high surface charge and hence were suitable for assembly.[26] We have used these particles to make colloidal crystal replica structures of semiconductors, magnetic materials, metals, and composite materials.[28–32]

The successful synthesis of these replica structures has enabled researchers to explore properties in 3D nanostructures in which the characteristic length scale of a physical phenomenon is comparable to the structural lattice parameter. The ability to control the size of silica nanoparticles in the sub-100 nm regime has also enabled systemic size-dependent studies in these nanostructures.[28]

Previous papers have discussed the effects of void size and ordering in the template colloidal crystalline films on the

structure and semiconducting, magnetic, acoustic, and plasmonic properties of replica materials.[28–32] Some of these properties are a function of the porosity of the structure, e.g., thermal transport, whereas others such as quantum confinement in semiconductors depend more on the pore size of the template. Transport properties such as electronic conductivity, and cooperative phenomena such as ferromagnetism are significantly affected by the interconnectivity and long-range order of the nanostructures. Therefore, understanding of the structures and degree of order in the nanoparticle templates is crucial to understanding and tuning the properties of the derived replicas.

The 3D structure of colloidal assemblies made from particles of different sizes and compositions has been characterized by real space imaging and by reciprocal space techniques. Real space imaging techniques include confocal microscopy,[33–35] FIB-SEM/TEM tomography,[36,37] and X-ray tomography/microscopy,[38–40]and reciprocal space techniques include light scattering (static, dynamic, small angle, multiple angle),[41–43] and X-ray scattering (small angle,[44–47] grazing incidence,[48–50] micro radian[51] and ultra-small angle[52–55]). Often real and reciprocal space techniques are used in combination as complementary techniques. The adequacy of the characterization technique is determined by the system characteristics (particle size, electron density contrast) and the problems being addressed (size determination, 3D structure, grain size, particle orientation, defects).

Light scattering and confocal microscopy for 3D structure determination are best suited for structures/particles in the hundreds of nanometers to several microns range due to diffraction limit of light. Electron/X-ray microscopy tomographic techniques extend into the sub-100 nm scale. They are useful in identifying the local crystal structure and defects. However, rigorous statistical analysis is required to determine average behavior at larger scale. X-ray scattering techniques provide information about structure and particle orientation averaged over several microns with particle sizes ranging from a few nanometers to a few microns. Therefore, grazing incidence and small angle X-ray scattering have been commonly used to study large scale structure and kinetics of nanoparticle superlattices.[56]

Silica colloidal crystals and their replicas in the micro- or nanometer regime have been studied previously by using light scattering,[57–61] confocal microscopy,[35] TEM/SEM,[61–64] X-ray tomography.[65] and SAXS.[60] The observed crystal structures include hcp/random hcp,[59,65] fcc,[57,58,64,66,67]and bcc,[57,58] depending on the particle size, inter-particle interaction, volume fraction, external forces (centrifugation, shear, electric field), substrate and deposition methods/conditions.

In this study, amino acid stabilized silica particles in the range of 20-125 nm have been synthesized and assembled into colloidal crystals. Earlier reports have shown that the amino acids facilitate hydrogen bonding between particles as they assemble allowing formation of ordered periodic structures as characterized by SEM.[26,27,63] Here we provide a detailed characterization of the structures of these colloidal materials and their replica by using small-angle X-ray scattering (SAXS) and SEM.

Results and discussion

As in earlier reports,[28,30,31,68] we used evaporation-driven vertical deposition[61] to assemble L-arginine capped silica nanoparticles into multilayer colloidal crystal films. As the solvent evaporates, particles accumulate at the solvent-air interface as shown in Figure S2. Slow evaporation (controlled by fixed temperature and humidity) results in the growth of ordered films.

Figure 1 shows top view SEM images of colloidal films assembled onto silicon wafer substrates. As in other evaporation-based assembly techniques, the drying of the films leads to crack formation, which can be easily seen in SEM images as shown in Figure S4. Boundaries separating grains of different orientations can also be observed (Figure 2). For example, regions marked 1 and 2 in Figure 2

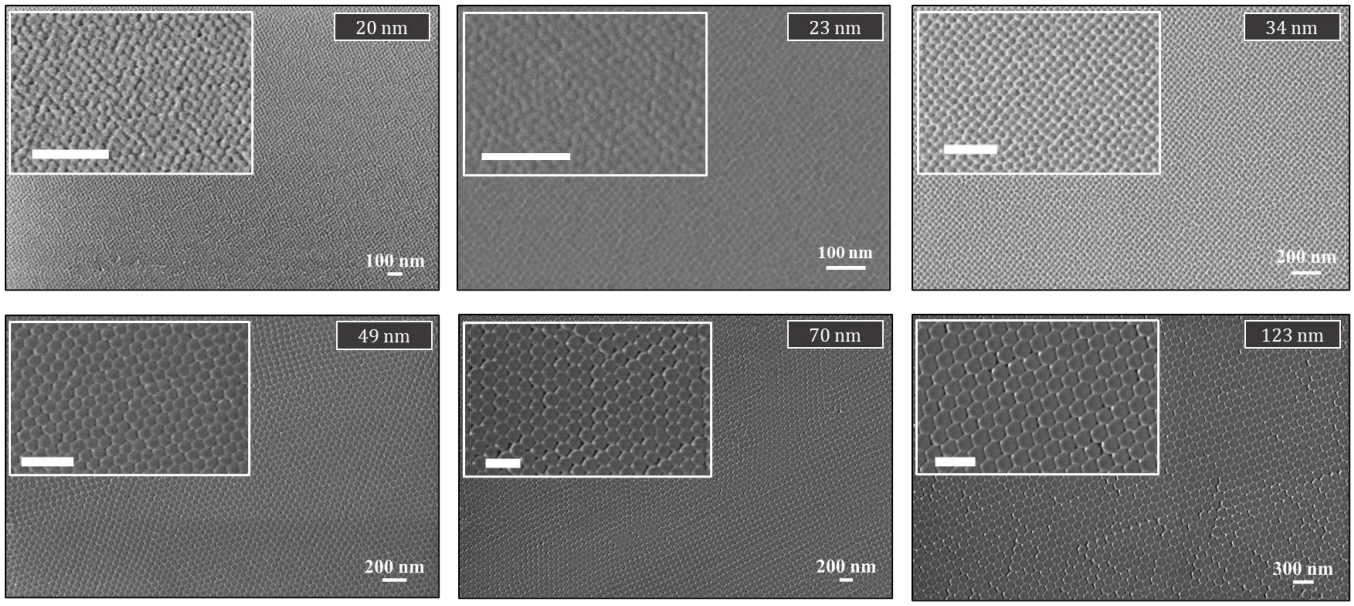

Figure 1. Top view of silica nanoparticles assembled as multilayer films on silicon substrates using the vertical deposition

technique. Inset images show magnified regions of the corresponding SEM images. The scale bars in the insets correspond to the same lengths as in their parent images.

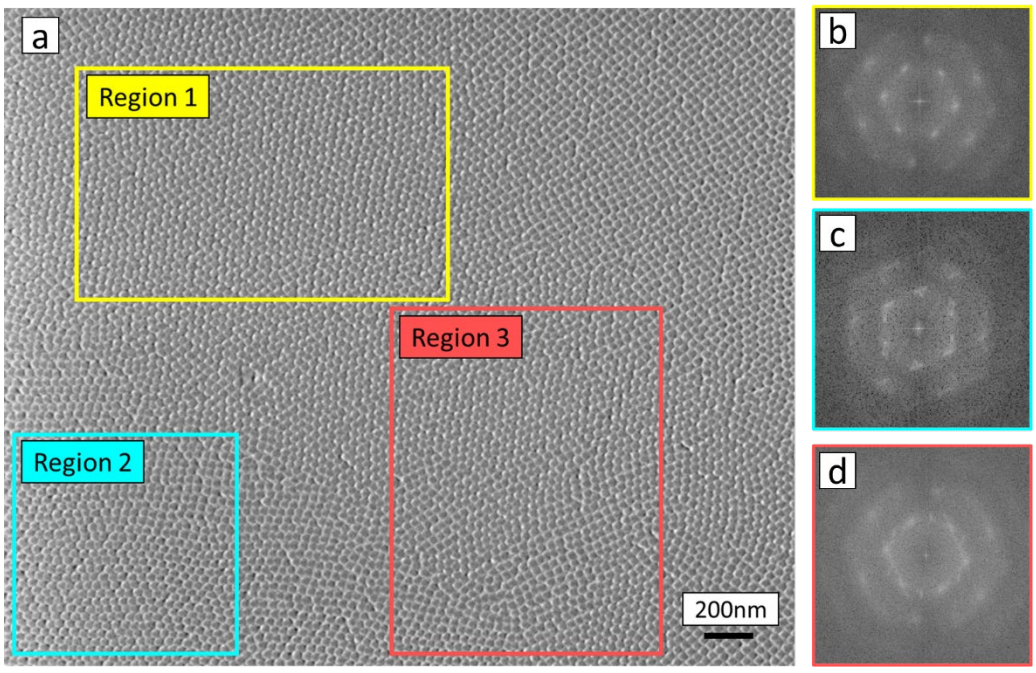

Figure 2. SEM images showing grain boundaries and different orientation of grains in a film of 34 nm silica spheres (a) SEM image of top view (b) FFT of region 1 marked in (a), (c) FFT of region 2 and (d) FFT of region 3. In both (a) and FFTs of the corresponding regions, different orientations of the grains can be identified. The grains in regions 1 and 2 appear at an angle of ~23° and region 3 contain multiple grains. Grains of different orientations were observed with other particle sizes as well.

have grains that are oriented at an angle of ~23° with respect to each other, and region 3 has a grain with both (or more) orientations as indicated by its corresponding fast Fourier transform (FFT) pattern. This polycrystalline texture is present in films of silica nanoparticles ranging from 20 to 123 nm diameter and can be identified in their SEM images. Other defects such as vacancies and twin boundaries are also observed in the assembled colloidal crystal films (Figure S4).

In the imaged 2D plane, the particles appear to be in a close-packed arrangement with apparent 6-fold symmetry that could represent 111, 0001 and/or 110 planes of face-centered cubic (fcc), hexagonal close-packed (hcp) and body-centered cubic (bcc) structures, respectively. However, the lack of 3D information in the SEM images and the limited two-dimensional views of the top surfaces of the multilayer films do not provide conclusive information about their bulk structures.

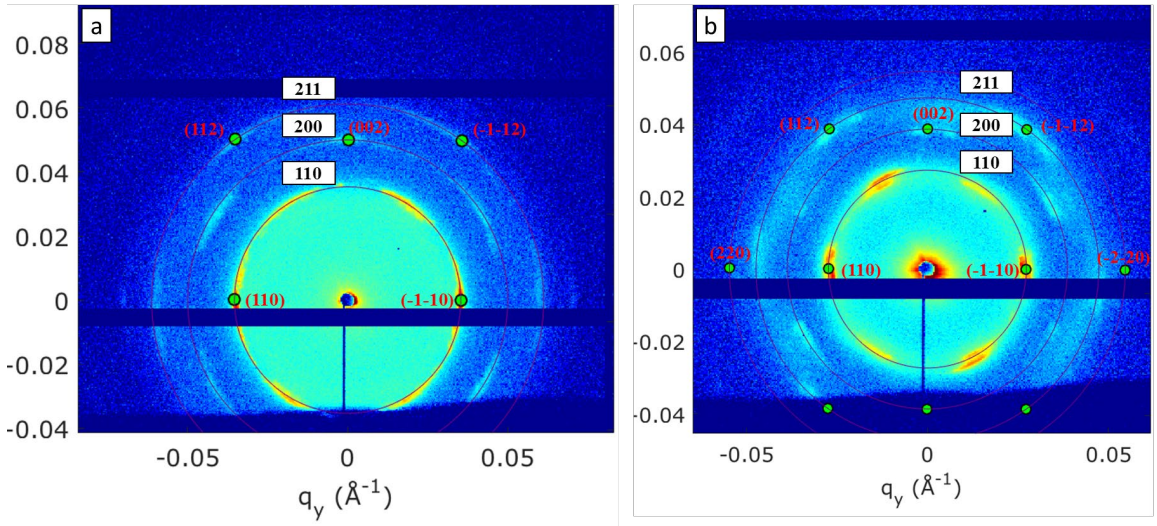

Figure 3. (a) 20.3 nm 2D scattering pattern with powder and single crystal fit showing bcc structure (a = 25.2 nm, 2r = 21.8 nm). (b) 23 nm 2D scattering pattern with powder and single crystal indexing showing bcc structure (a = 32.5, 2r = 28.2 nm). Rotations of the orientation of crystallites in the 2D plane explain all the diffraction spots. (Figure S5)

In SAXS, using a beam spot of 200 x 100 μm², a much larger region is interrogated and the 3D arrangement of particles throughout the film (300 nm - 1.5 μm) contributes to the scattering pattern. Thus, 2D SAXS patterns collected in transmission contain information about the structure, orientation and crystallinity of the colloidal crystal films. We identified representative 2D patterns for each nanoparticle size from scattering patterns of multiple spots in the same sample and/or from multiple samples grown under the same conditions.

Figure 3 shows representative 2D scattering patterns for 20.3 and 22.7 nm silica particle templates. The scattering patterns can be explained by using bcc structure with lattice parameters of 25.2 and 32.5 nm for the 20.3 and 22.7 nm templates, respectively. The rings in the 2D patterns represent bcc structure 3D powders without specific orientations. However, the 2D patterns of the templates also contain bright spots that can be explained by indexing them to oriented single crystals. The indexing of some of these reflections is shown in Fig. 3, however all of them can be indexed by in plane rotations of this single crystal orientation (Figure S5). This implies the presence of multiple crystallites at different angles in the 2D plane with bcc as their 3D structure. Other 2D scattering patterns observed for these two sizes are shown and indexed in the bcc structure in Figures S6 and S7.

For sizes larger than 22.7 nm, we use combination of 2D scattering patterns and their azimuthally averaged 1D patterns to determine the 3D crystal structure. Figure 4 shows 2D hexagonal indexing for 48.8, 69.7 and 122.7 nm templates. The 2D patterns can be indexed using 2D hexagonal system space group p6mm with close pack plane orientation perpendicular to the X-ray beam. The reflections which are not indexed in Figure 4 are indexed by rotation of the crystallite in the 2D plane as shown in Figure S8.

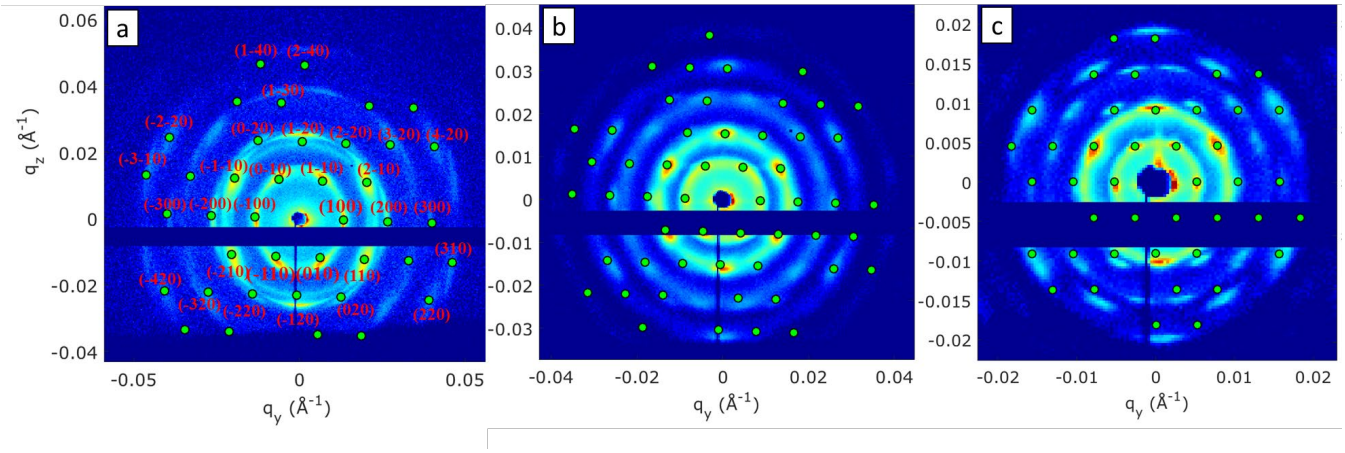

Figure 4. 2D hex fit using p6mm space-group and orientation of close pack plane perpendicular to the beam direction (a) 48.8 nm, a = 54.4 (b) 69.7 nm, a = 82.5 nm and (c) 122.7 nm, a = 137.7 nm. The indexing of reflections is same for (a), (b) and (c). The reflections not indexed here can be explained by a different crystallite orientation in the 2D plane as shown in Figure S8.

The indexed 2D scattering patterns were used to extract the lattice parameter for these templates. In order to understand the 3D arrangement of the close pack planes in these templates, azimuthally averaged 1D scattering patterns of simulated close pack structures were compared with the 1D patterns of the templates. Figure 5a shows the simulated 1D patterns for 5 different oriented close pack structures – face centered cubic (fcc), hexagonal close pack (hcp), 2D hexagonal (HEX) and random hexagonal close pack (rhcp).

2D hexagonal represents a 2D close pack structure labelled as A/B/C. In fcc structure, the stacking of close pack planes is ABCABC and the 111 plane is perpendicular to the beam. Likewise, for hcp structure the 100 plane is perpendicular to the x ray beam and the stacking is ABABA. In rhcp structures this stacking of close pack planes (A/B/C) is random. Figure 5a has two types of rhcp structures where rhcp1 considers the peak shape is still round and rhcp2 assumes the peak shape elongation along the qz axis.

The 1D patterns obtained by azimuthal averaging of the simulated 2D patterns (Figure S11) highlight the difference between different oriented close pack structures. The first reflections observed in fcc is the one at $\frac{qD}{2\pi} = 2$, corresponding to the position of {110} of 2D hexagonal. In hcp, the peak that corresponds to {100} reflection of 2D hexagonal shows up. The major difference between various structures is the relative peak intensity of the first two reflections {100} and {110} reflections. 2D hexagonal shows the highest {100} peak intensity followed by hcp. The rhcp could show any intensity between hcp and fcc depending on the degree of randomness. If there is no registration along the Z axis at all, for example if an AA stacking can occur, rhcp would be no different from 2D hexagonal. The 1D patterns for templates were adjusted by the lattice parameter obtained from the 2D indexed patterns to overlay with the simulated 1D patterns. From Figure 5b, it is evident that the template structure is not fcc. In order to distinguish between the remaining structures, peak 1: peak 2 ratio was compared. Table S2 shows the peak ratios for different simulated close pack structures and the different size silica templates. The peak ratios for 31.1 nm, 69.7 nm and 122.7 nm are between rhcp1 and rhcp2. 48.8 nm has ratio between rhcp2 and hcp. These values indicate that the particles assemble in rhcp structure with possible peak shape elongation along qz axes. This elongation is also observed in the 2D scattering patterns. However, the reflections are predominantly broad as seen in both 1D/2D patterns indicating presence of 2D hexatic phase[69]. Some sharp reflections are also present for

example in 48.8 nm ~ q = 1, 2.04 Å^{-1} which indicate crystalline behavior.

Thus, the smaller sizes 20.3 nm and 22.7 nm assemble into non-close pack body centered cubic structure and sizes 48.8 ,69.7 and 122.7 nm assemble into random hexagonal close pack structure with 2D hexatic phase. The larger sizes have short range translational order and in contrast, smaller sizes have long range translational order (sharp reflections). In this trend, 31.1 nm is the transition size, its 1D pattern shows similarity with rhcp1 structure but there are reflections which cannot be explained by just one structure. These could be multiple structures as shown in Figure S12. The lattice parameter from SAXS for 31.1 nm template is reported corresponding to a p6mm indexing as done for other larger sizes.

There are several factors (both kinetic and thermodynamic)[70–74] that determine the final structure of a colloidal crystal film made by evaporative assembly of charged nanoparticles. The interplay of these parameters is complex and

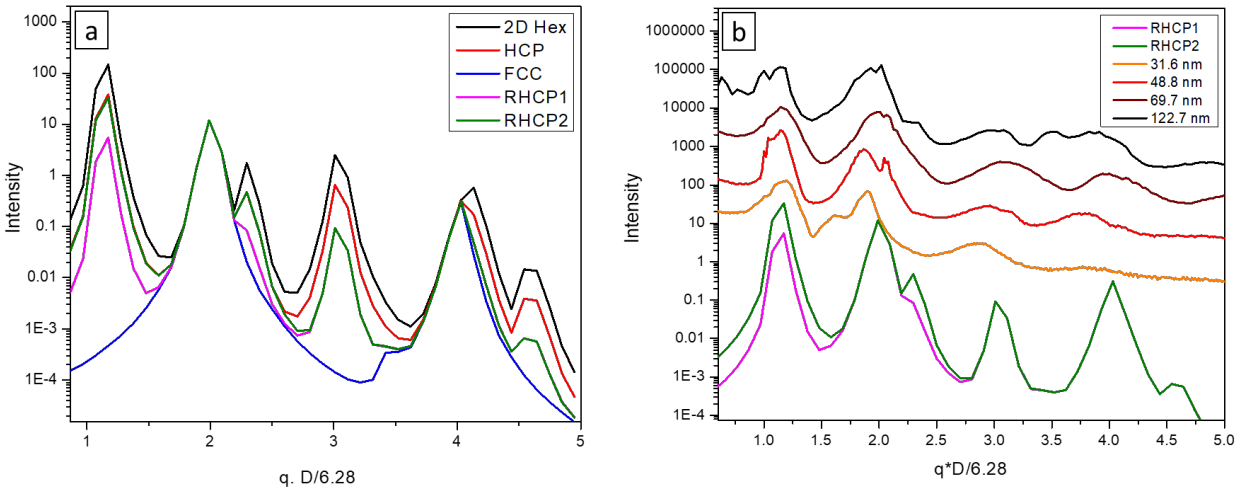

Figure 5. (a) Simulated azimuthally averaged 1D patterns of different oriented close pack structures. Corresponding 2D patterns are in Figure S11. (b) Comparison of azimuthally averaged 1D patterns of different sizes with the simulated 1D patterns shown in (a) and Figure S12. Particle size is calculated from the lattice parameter in the SAXS for consistency.

so, it is non-trivial to evaluate each independently. However, we can qualitatively evaluate some of the dominant factors in our system such as charged based repulsion, polydispersity, vanderwaal attraction and shear. Body centered cubic structures for spherical systems are favored when there is long range repulsion[75–77], high dispersity[78,79] and are also formed due to shear induced transition from close pack structures[80,81]. Further investigation is needed to determine their independent influence and combined interplay on the assembly in this study. We have evidence of higher polydispersity in smaller (20.3, 22.7 nm) sizes compared to larger size (Table S1). The standard deviation in smaller sizes (20.3 and 22.7 nm) was found to be around 5-6.5% whereas for larger sizes it was lower than 4-5%. This high dispersity could be a contributing factor for formation of bcc structure. The transition size in this trend, 31.1 nm, also has high dispersity which could be the reason behind its complex behavior with multiple structures.

For larger sizes, the rhcp structure of a 2D hexatic phase is observed. This behavior is common in sheared spherical colloids. During the vertical deposition process, the particles experience shear, which is known to cause slipping of planes leading to random stacking.[82] Increased attraction between the larger particles potentially leads to short-range translational order/2D hexatic phase behavior in these hexagonally packed layers.

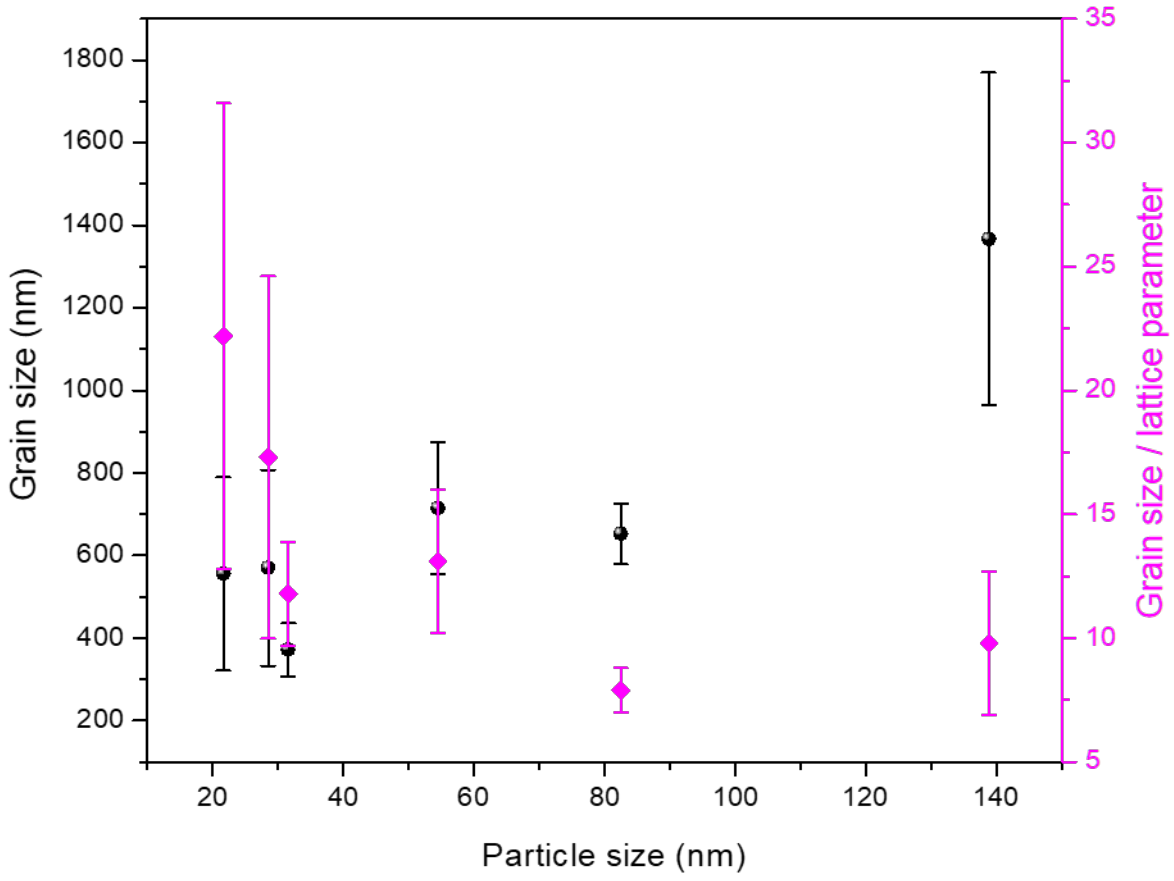

Figure 6. Variation in grain size and number of unit cells in a grain as a function of particle size.

This is also reflected in the subtle variation of the number of unit cells in an average grain as a function of particle size. The grain sizes were determined using the full width at half-maximum (FWHM) of the first order reflections and the Debye Scherrer equation (See SI for details of the calculation) for different size nanoparticle templates. The average number of unit cells in an average grain shows a gradual decrease with the increasing particle size (Figure 6). This trend supports the decrease in the translational order in the templates with increasing size as previously discussed. However, a significant variation is observed in the grain size for all sizes. Grain sizes are known to be influenced by particle size dispersity and by deposition conditions.[83,84]

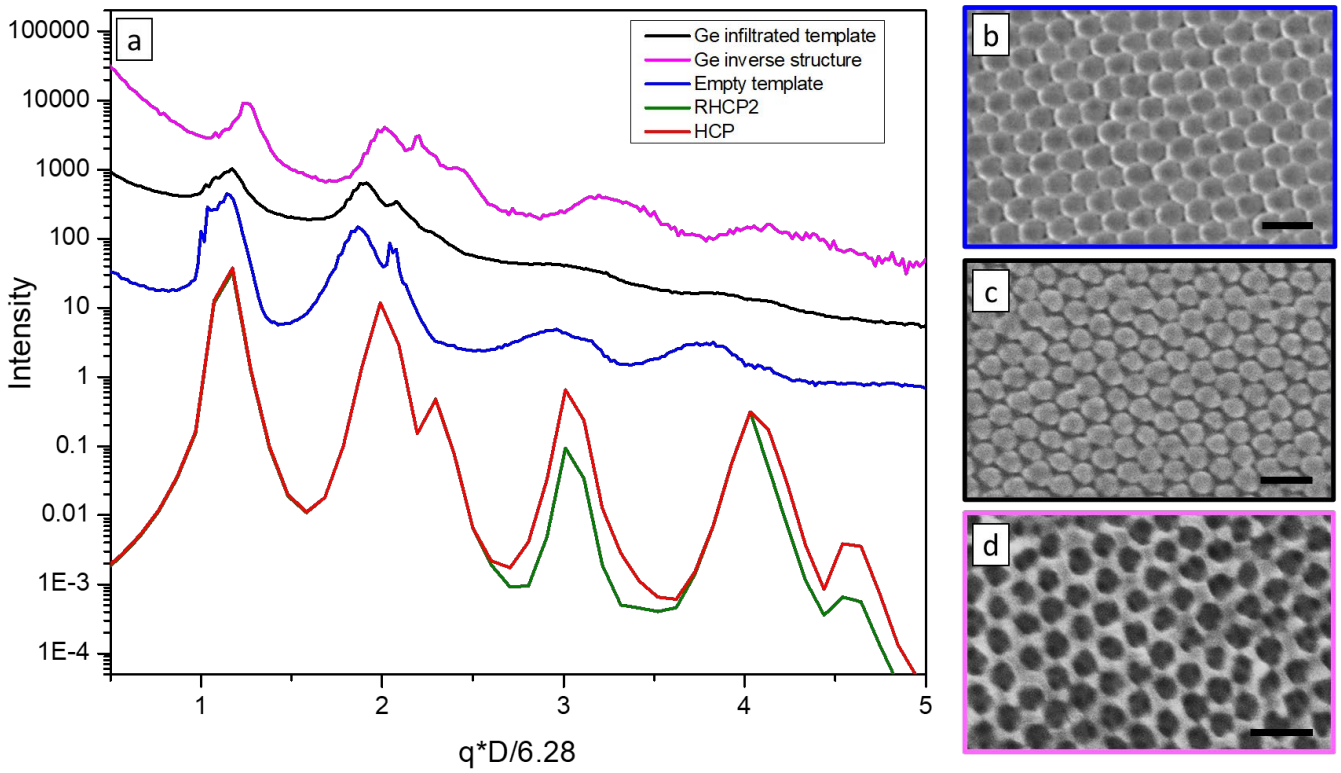

Figure 7. (a) Comparison of azimuthally averaged 1D patterns for 48.8 nm empty template, Ge infiltrated template and Ge inverse structure after template removal with simulated 1D patterns for rhcp and hcp. Representative SEM images (top view) of (b) empty silica template film (c) Ge-infiltrated template film and (d) inverse Ge structure. Inset scale bar in SEM images is 100 nm.

SEM images also show grain boundaries and defects in proximity to anomalously sized particles, as shown in Figure S4. Narrower particle size distributions and a controlled rate of deposition can help to lower the variation in grain size and further decrease the density of grain boundaries. Both large grains and uniform grain sizes are desirable for certain applications of colloidal crystals and their replicas.

The voids in these colloidal crystal films can be infiltrated using high-pressure confined chemical vapor deposition (HPcCVD) and high-pressure supercritical fluid deposition (HPCFD) with semiconductors and metals as shown for 48.8 nm template films in Figure 7. In order to understand the properties of these 3D nanostructures independent of the template, we used HF to selectively etch away the silica nanoparticles. SEM images after etching confirm the formation of an interconnected Ge nanostructure as shown in Figure 7d. TEM tomography of these systems reported previously has analyzed the variation in structure between different voids and interconnections.[85] However, as previously discussed, this information in limited to a small region or field of view in the TEM. Since the nanostructure only occupies ~26-32% of the film volume, it is important to confirm the preservation of the long-range structure and ordering in the replica films after template etching.

Figure 7 shows 1D SAXS patterns for a 48.8 nm silica film template, the Ge infiltrated film, and the Ge nanostructure following template etching. We chose Ge rather than Si for this study due its contrast with silica in the SAXS measurement. The 48.8 nm infiltrated template and inverse Ge structure also show a similar structure to the template. The peak1: peak 2 ratios in infiltrated and inverse structures are between simulated rhcp1 and rhcp 2. Thus, akin to the template, these also have rhcp structure with broad reflections indicating presence of 2D hexatic phase. There indexed 2D patterns are shown in Figure S14.

This behavior of inheriting template structure is observed in other sizes as well. For smaller sizes, 20.3 and 22.7 nm, inverse Ge also shows bcc structure like their corresponding templates as shown in Figure S15. In case of 31.1, 69.7 and 122.7 nm, rhcp structure is formed with peak1: peak 2 ratios varying between rhcp1 and hcp simulated structures indicating different stacking patterns and elongation along z axes (Table S5 and Figure S17). In these larger sizes, just like their templates, presence of 2D hexatic phase is observed in the form of broad reflections. This comparison confirms the retention of structure following semiconductor infiltration and template etching.

Conclusions. Sub-100 nm monodisperse silica nanoparticles have been synthesized and assembled into 3D

structures as films using evaporation induced vertical deposition. These nanoparticle films were used as templates and infiltrated with germanium to obtain a 3D interconnected replica. Using SEM and SAXS, we have characterized the structure and ordering of the silica nanoparticle templates and the replica materials derived from them.

From SEM images, information on particle size and shape, their relative arrangement in the 2D plane, crystallinity and type of defects was obtained. The particles are spherical in shape with standard deviations in particle size within 6.5%, and appear to be in close packed arrangements within the 2D surface plane. Several SEM images show grains with different orientations in all the films indicating polycrystallinity. Other defects such as vacancies and cracks due to drying of the films were also observed in SEM images.

More detailed information about the 3D arrangement of the particles could be obtained by SAXS. A size-dependent variation was observed in the colloidal crystal silica films. Particles smaller than 31.1 nm assembled into the non-close packed bcc structure, whereas particles larger than 31.1 nm assemble into random hexagonal close pack with 2D hexatic phase.

We extended this analysis to the infiltrated templates and replica nanostructures after template removal. Using SAXS, we confirmed that the high temperature and pressure infiltration of the template does not affect its structure or ordering. After etching, the replica material retains the template structure.

This study confirms that silica nanoparticle assembly forms a robust model system for template-mediated design of 3D interconnected and periodic nanostructures on the sub-100 nm length scale. A detailed understanding of particle arrangements in the template can help in establishing structure-property relationships in the replica nanostructures. The formation of non-close-packed structures without the use of specific ligand interaction or substrate modification can likely be attributed to particle size dispersity and shear forces in the assembly process. These parameters can in principle be tuned to obtain different structures as needed.

Methods

Silica nanoparticle synthesis and assembly. Monodisperse silica nanoparticles of 20 to 125 nm diameter were synthesized by using the method described by Hartlen *et al*.[26] and Watanbe *et al*,[27] as discussed in detail by Russell[68]. The synthesis involves base-catalyzed hydrolysis of a silica precursor, tetraethylorthosilicate (TEOS), in an aqueous medium. Both approaches can be applied to the synthesis of nanoparticles between 14-200 nm diameter, and the seed-regrowth approach can be used to obtain larger sizes. However, they implemented different strategies to gain control of the size and dispersity. Hartlen's approach includes a two-phase reaction with a floating organic layer of cyclohexane to slowly add TEOS to the aqueous reaction mixture. The cyclohexane does not participate in the reaction but slows down the hydrolysis of TEOS, providing control over the nucleation and growth rate of the particles. In the Watanabe synthesis, the organic layer is absent and ethanol is used as co-solvent in the regrowth steps to obtain larger particle sizes.

We used the Watanabe method for synthesis of 20.3 nm, 69.7 nm and 122.7 nm diameter particles and the Hartlen method for synthesis of 22.7, 31.1, 48.8 nm particles. All reagents were purchased from Sigma Aldrich and nanopure water (Barnstead) was used for synthesis. Table S1 summarizes the type of reaction, concentration of the reagents used for the synthesis, reaction conditions and deposition conditions. A brief description for both types of reactions is provided below and a schematic is shown in Figure S1:

(a) One phase synthesis – 20.3 nm particles were prepared by mixing 0.49 mmol of L-arginine, 4.8 mol of water and 25 mmol of TEOS in a round bottom flask under constant stirring. The mixture was heated at 70° C for 24 hours. These particles were used as seeds for the synthesis of 69.7 nm and 122.7 nm particles in a similar one phase reaction. Briefly, for 122.7 nm particles, 0.27 g of seed solution was added to 1.2 mol of water, 1.5 mol of ethanol containing 0.5 mol of L-arginine and 25 mmol of TEOS in a round bottom flask. This solution was heated at 70° C for 24 hours. A similar procedure was followed with different concentrations for the synthesis of 69.7 nm particles as given in Table S1.

(b) Two phase synthesis - For the synthesis of ~22.7 nm particles, a solution of 3.8 mol of water and 0.52 mmol of L-arginine was prepared in a round bottom flask and maintained with constant stirring. A floating layer of 0.042 mol cyclohexane was slowly added to the top of this aqueous solution and the reaction mixture was heated to 60° C. Once the final temperature was reached, 25 mmol of TEOS was added to the cyclohexane layer slowly and dropwise. The reaction was allowed to continue for 20 hours. These particles were used as seeds for the synthesis of 31.1 and 48.8 nm particles. Briefly, for 31.1 nm particles, 20 mL of seed solution was added to 4 mol of water in a round bottom flask under constant stirring. A floating layer of 0.09 mol of cyclohexane was added to the solution and heated to 60° C before dropwise addition of 32 mmol of TEOS. The reaction was left undisturbed for 30 hours. 48.8 nm particles were obtained by increasing the reaction time to 48 hours with the same reaction mixture.

Vertical deposition for particle assembly –Nanoparticle films were prepared using the vertical deposition technique described by Russell *et al*[68,86]. Briefly, silicon wafers (University Wafers) of ~280 μm thickness and <100> orientation were used as substrates for the colloidal film growth. The wafers were cut into 3 cm x 1cm pieces and were pretreated with piranha solution (3:1 concentrated H_2SO_4: 30% v/v H_2O_2) for 15-20 minutes and rinsed with water before deposition. [*Note:* Piranha solution is corrosive and can react violently with organic substances]

The as-prepared silica nanoparticle solutions were diluted to 10x (122.7 nm, 69.7 nm and 48.8 nm) and 7.5x (20.3 nm, 22.7 nm and 31.1 nm) for deposition without any further purification. The Si wafers were immersed in the nanoparticle solution at a 30° angle in open plastic vials as shown in Figure S2. These vials were left undisturbed for 2 weeks in a temperature- and humidity-controlled oven. Sizes 20.3, 22.7, 31.1, 48.8 and 69.7 nm were deposited at 40 °C with 82% relative humidity (RH). 122.7 nm particles were deposited at 45 °C and 75-80% RH. The RH was controlled by placing an open crystallizing dish containing an appropriate concentration of NaCl in water in the oven.

The thickness of the films varied between 300 nm – 1.5 micron depending on the nanoparticle size and the position in

the substrate. Figure S3 shows a cross sectional view of films derived from 20.3 nm and 122.7 nm particles. Smaller nanoparticle sizes tended to result in thicker films.

Infiltration of germanium into the colloidal crystalline films and template etching - High Pressure confined Chemical Vapor Deposition (HPcCVD) was used to fabricate germanium replicas using a 5 - 10% partial pressure of germane in helium carrier gas with total pressure of 25 - 30 MPa. Template films were kept 25 μm apart to ensure spatial confinement in the HPcCVD reactor. Germanium was infiltrated at 325 °C with deposition time ranging from 1 - 3 hours depending on template particle size, germane partial pressure and total pressure of the system. An overlayer of germanium was formed during infiltration after voids in the template were fully filled. The overlayer was removed using chlorine-based reactive ion etching (RIE). To prepare germanium replicas without the nano-template, the infiltrated sample was treated with an aqueous 3% HF solution to selectively remove silica, followed by a water and acetone rinse.

Scanning electron microscopy – Silica nanoparticles and films were imaged using a Zeiss SIGMA VP-FESEM and Quanta SEM. The particle size analysis was done using Image J software. 50 nanoparticles were measured to obtain each size distribution. For smaller sizes, due to lower image resolution, three particles were measured to obtain the mean size and standard deviation.

Small Angle X-ray Scattering – Transmission SAXS measurements were performed at Advanced Photon source, Argonne National Lab (Beamline 12-ID-B). A spot size of 200 x 100 μm^2 of 14 keV X-rays was used with 1s exposure time to collect 2D patterns on a Pilatus 2M detector. Several 2D patterns across different regions on the samples and replica structures were recorded.

2D patterns were indexed assuming densest layer is parallel to the substrate. Azimuthal averaging was done to obtain 1D patterns. Details of close pack structure simulation are included in the supplementary information.

ASSOCIATED CONTENT

The supporting information is available free of charge via the Internet at http://pubs.acs.org. Details on reaction conditions, cross sectional SEM images of 20 nm and 123 nm templates, SEM images showing different regions of 123 nm template highlighting different types of defects. Table containing details on structure, lattice parameter and grain size for different templates. Representative 1D and 2D SAXS patterns for 23 nm, 70 nm and 123 nm with fit for different structures in 1D pattern, SEM image comparing compositional softness induced shape ripening in 34 nm and 123 nm films. Representative 1D SAXS patterns of inverse opal Ge films after silica template removal

AUTHOR INFORMATION

Corresponding Author

Pratibha Mahale - Department of Chemistry, University of Pennsylvania, Philadelphia, Pennsylvania 19104, United States; Email: pmahale@sas.upenn.edu

Author Contributions

P.M., H.Y.C and B. L. designed the study in consultation with T.E.M. P. M., H.Y.C and B. L. carried out the experimental work, and all authors contributed to the analysis of the data. The manuscript was drafted by P.M. and edited by all authors.

ACKNOWLEDGMENTS

PM would like to thank Saiphaneedra Bachu and Disha Talreja for discussions. This work was supported by the National Science Foundation under MRSEC grant DMR-1420620. This research used resources of the Advanced Photon Source, a U.S. Department of Energy (DOE) Office of Science User Facility operated for the DOE Office of Science by Argonne National Laboratory under contract DE-AC02-06CH11357.

ABBREVIATIONS

SAXS, small angle X-ray scattering; HPcCVD, high pressure confined chemical vapor deposition; HPcCFD, high pressure confined chemical fluid deposition.

REFERENCES

(1) Talapin, D. V.; Lee, J. S.; Kovalenko, M. V.; Shevchenko, E. V. Prospects of Colloidal Nanocrystals for Electronic and Optoelectronic Applications. *Chem. Rev.* **2010**, *110* (1), 389–458.

(2) Manoharan, V. N. Colloidal Matter: Packing, Geometry, and Entropy. *Science*. **2015**, 349, 6251.

(3) Kumar, S. K.; Kumaraswamy, G.; V Prasad, B. L.; Bandyopadhyaya, R.; Granick, S.; Gang, O.; Manoharan, V. N.; Frenkel, D.; Kotov, N. A. *Nanoparticle Assembly: A Perspective and Some Unanswered Questions*; 2017; Vol. 112. 1635-1641.

(4) Boles, M. A.; Engel, M.; Talapin, D. V. Self-Assembly of Colloidal Nanocrystals: From Intricate Structures to Functional Materials. *Chemical Reviews*. American Chemical Society September 28, 2016, pp 11220–11289.

(5) Li, F.; Josephson, D. P.; Stein, A. Colloidal Assembly: The Road from Particles to Colloidal Molecules and Crystals. *Angew. Chemie Int. Ed.* **2011**, *50* (2), 360–388.

(6) Pellegrino, T.; Kudera, S.; Liedl, T.; Muñoz Javier, A.; Manna, L.; Parak, W. J. On the Development of Colloidal Nanoparticles towards Multifunctional Structures and Their Possible Use for Biological Applications. *Small* **2004**, *1* (1), 48–63.

(7) Glotzer, S. C.; Solomon, M. J.; Kotov, N. A. Self-Assembly: From Nanoscale to Microscale Colloids. *AIChE J.* **2004**, *50* (12), 2978–2985.

(8) Liguang Xu; Wei Ma; Libing Wang; Chuanlai Xu; Hua Kuang; A. Kotov, N. Nanoparticle Assemblies: Dimensional Transformation of Nanomaterials and Scalability. *Chem. Soc. Rev.* **2013**, *42* (7), 3114–3126.

(9) Derrien, T. L.; Hamada, S.; Zhou, M.; Smilgies, D. M.; Luo, D. Three-Dimensional Nanoparticle Assemblies with Tunable Plasmonics via a Layer-by-Layer Process. *Nano Today* **2020**, *30*, 100823.

(10) Park, J.; Hickey, D. R.; Jun, S.; Kang, S.; Hu, X.; Chen, X.-J.; Park, S.-J. Surfactant-Assisted Emulsion Self-Assembly of Nanoparticles into Hollow Vesicle-Like Structures and 2D Plates. *Adv. Funct. Mater.* **2016**, *26* (43), 7791–7798.

(11) Majewski, P. W.; Michelson, A.; Cordeiro, M. A. L.; Tian, C.; Ma, C.; Kisslinger, K.; Tian, Y.; Liu, W.; Stach, E. A.; Yager, K. G.; Gang, O. Resilient Three-Dimensional Ordered Architectures Assembled from Nanoparticles by DNA. *Sci. Adv.* **2021**, *7* (12), eabf0617.

(12) Choi, J. J.; Bealing, C. R.; Bian, K.; Hughes, K. J.; Zhang, W.; Smilgies, D.-M.; Hennig, R. G.; Engstrom, J. R.; Hanrath, T. Controlling Nanocrystal Superlattice Symmetry and Shape-Anisotropic Interactions through Variable Ligand Surface Coverage. *J. Am. Chem. Soc.* **2011**, *133* (9), 3131–3138.

(13) Shields, C. W.; Velev, O. D. The Evolution of Active Particles: Toward Externally Powered Self-Propelling and Self-Reconfiguring Particle Systems. *Chem* **2017**, *3* (4), 539–559.

(14) Johnson, S. A.; Ollivier, P. J.; Mallouk, T. E. *Ordered Mesoporous*

Polymers of Tunable Pore Size from Colloidal Silica Templates; 1991; Vol. 74.963-965.

(15) Yan, H.; Blanford, C. F.; Holland, B. T.; Parent, M.; Smyrl, W. H.; Stein, A. A Chemical Synthesis of Periodic Macroporous NiO and Metallic Ni. *Adv. Mater.* **1999**, *11* (12), 1003–1006.

(16) Braun, P. V.; Wiltzius, P. Electrochemically Grown Photonic Crystals. *Nature* **1999**, *402* (6762), 603–604.

(17) Vlasov, Y. A.; Yao, N.; Norris, D. J. Synthesis of Photonic Crystals for Optical Wavelengths from Semiconductor Quantum Dots. *Adv. Mater.* **1999**, *11* (2), 165–169.

(18) Zakhidov, A. A.; Baughman, R. H.; Iqbal, Z.; Cui, C.; Khayrullin, I.; Dantas, S. O.; Marti, J.; Ralchenko, V. G. Carbon Structures with Three-Dimensional Periodicity at Optical Wavelengths. *Science (80-.).* **1998**, *282* (5390), 897–899.

(19) Gates, B.; Yin, Y.; Xia, Y. Fabrication and Characterization of Porous Membranes with Highly Ordered Three-Dimensional Periodic Structures. *Chem. Mater.* **1999**, *11* (10), 2827–2836.

(20) Velev, O. D.; Jede, T. A.; Lobo, R. F.; Lenhoff, A. M. Porous Silica via Colloidal Crystallization [9]. *Nature*. Nature Publishing Group 1997, pp 447–448.

(21) Nicholas A. Kotov,; Yuanfang Liu,; Shaopeng Wang, §; Colin Cumming ; Mohammad Eghtedari, Gracie Vargas, Massoud Motamedi, Joan Nichols, and; Cortiella, J. Inverted Colloidal Crystals as Three-Dimensional Cell Scaffolds. *Langmuir* **2004**, *20* (19), 7887–7892.

(22) Stöber, W.; Fink, A.; Bohn, E. Controlled Growth of Monodisperse Silica Spheres in the Micron Size Range. *J. Colloid Interface Sci.* **1968**, *26* (1), 62–69.

(23) Osseo-Asare, K.; Arriagada, F. J. Preparation of SiO2 Nanoparticles in a Non-Ionic Reverse Micellar System. *Colloids and Surfaces* **1990**, *50* (C), 321–339.

(24) Arriagada, F. J.; Osseo-Asare, K. Synthesis of Nanosize Silica in a Nonionic Water-in-Oil Microemulsion: Effects of the Water/Surfactant Molar Ratio and Ammonia Concentration. *J. Colloid Interface Sci.* **1999**, *211* (2), 210–220.

(25) Yokoi, T.; Wakabayashi, J.; Otsuka, Y.; Fan, W.; Iwama, M.; Watanabe, R.; Aramaki, K.; Shimojima, A.; Tatsumi, T.; Okubo, T. Mechanism of Formation of Uniform-Sized Silica Nanospheres Catalyzed by Basic Amino Acids. *Chem. Mater.* **2009**, *21* (15), 3719–3729.

(26) Hartlen, K. D.; Athanasopoulos, A. P. T.; Kitaev, V. Facile Preparation of Highly Monodisperse Small Silica Spheres (15 to >200 nm) Suitable for Colloidal Templating and Formation of Ordered Arrays. *Langmuir* **2008**, *24* (5), 1714–1720.

(27) Watanabe, R.; Yokoi, T.; Kobayashi, E.; Otsuka, Y.; Shimojima, A.; Okubo, T.; Tatsumi, T. Extension of Size of Monodisperse Silica Nanospheres and Their Well-Ordered Assembly. *J. Colloid Interface Sci.* **2011**, *360* (1), 1–7.

(28) Chen, W.; Talreja, D.; Eichfeld, D.; Mahale, P.; Nova, N. N.; Cheng, H. Y.; Russell, J. L.; Yu, S.-Y.; Poilvert, N.; Mahan, G.; Mohney, S. E.; Crespi, V. H.; Mallouk, T. E.; Badding, J. V.; Foley, B.; Gopalan, V.; Dabo, I. Achieving Minimal Heat Conductivity by Ballistic Confinement in Phononic Metalattices. *ACS Nano* **2020**, 14(4), 4235-4243.

(29) Abad, B.; Knobloch, J. L.; Frazer, T. D.; Hernández-Charpak, J. N.; Cheng, H. Y.; Grede, A. J.; Giebink, N. C.; Mallouk, T. E.; Mahale, P.; Nova, N. N.; Tomaschke, A. A.; Ferguson, V. L.; Crespi, V. H.; Gopalan, V.; Kapteyn, H. C.; Badding, J. V.; Murnane, M. M. Nondestructive Measurements of the Mechanical and Structural Properties of Nanostructured Metalattices. *Nano Lett.* **2020**, *20* (5), 3306–3312.

(30) Mahale, P.; Moradifar, P.; Cheng, H. Y.; Nova, N. N.; Grede, A. J.; Lee, B.; De Jesús, L. R.; Wetherington, M.; Giebink, N. C.; Badding, J. V.; Alem, N.; Mallouk, T. E. Oxide-Free Three-Dimensional Germanium/Silicon Core-Shell Metalattice Made by High-Pressure Confined Chemical Vapor Deposition. *ACS Nano* **2020**, 14(10),12810-12818.

(31) Liu, Y.; Kempinger, S.; He, R.; Day, T. D.; Moradifar, P.; Yu, S. Y.; Russell, J. L.; Torres, V. M.; Xu, P.; Mallouk, T. E.; Mohney, S. E.; Alem, N.; Samarth, N.; Badding, J. V. Confined Chemical Fluid Deposition of Ferromagnetic Metalattices. *Nano Lett.* **2018**, *18* (1), 546–552.

(32) Chen, Y.; Liu, Y.; Moradifar, P.; Glaid, A. J.; Russell, J. L.; Mahale, P.; Yu, S. Y.; Culp, T. E.; Kumar, M.; Gomez, E. D.; Mohney, S. E.; Mallouk, T. E.; Alem, N.; Badding, J. V.; Liu, Y. Quantum Transport in Three-Dimensional Metalattices of Platinum Featuring an Unprecedentedly Large Surface Area to Volume Ratio. *Phys. Rev. Mater.* **2020**, *4* (3), 035201.

(33) Mohraz, A.; Solomon, M. J. Direct Visualization of Colloidal Rod Assembly by Confocal Microscopy. *Langmuir* **2005**, *21* (12), 5298–5306.

(34) Varadan, P.; Solomon, M. J. Direct Visualization of Long-Range Heterogeneous Structure in Dense Colloidal Gels. *Langmuir* **2003**, *19* (3), 509–512.

(35) Van Blaaderen, A.; Wiltzius, P. Real-Space Structure of Colloidal Hard-Sphere Glasses. *Science.* **1995**, *270* (5239), 1177–1179.

(36) Van Der Hoeven, J. E. S.; Van Der Wee, E. B.; De Winter, D. A. M.; Hermes, M.; Liu, Y.; Fokkema, J.; Bransen, M.; Van Huis, M. A.; Gerritsen, H. C.; De Jongh, P. E.; Van Blaaderen, A. Bridging the Gap: 3D Real-Space Characterization of Colloidal Assemblies via FIB-SEM Tomography. *Nanoscale* **2019**, *11* (12), 5304–5316.

(37) Boneschanscher, M. P.; Evers, W. H.; Qi, W.; Meeldijk, J. D.; Dijkstra, M.; Vanmaekelbergh, D. Electron Tomography Resolves a Novel Crystal Structure in a Binary Nanocrystal Superlattice. *Nano Lett.* **2013**, *13* (3), 1312–1316.

(38) Hilhorst, J.; Van Schooneveld, M. M.; Wang, J.; De Smit, E.; Tyliszczak, T.; Raabe, J.; Hitchcock, A. P.; Obst, M.; De Groot, F. M. F.; Petukhov, A. V. Three-Dimensional Structure and Defects in Colloidal Photonic Crystals Revealed by Tomographic Scanning Transmission x-Ray Microscopy. *Langmuir* **2012**, *28* (7), 3614–3620.

(39) Furlan, K. P.; Larsson, E.; Diaz, A.; Holler, M.; Krekeler, T.; Ritter, M.; Petrov, A. Y.; Eich, M.; Blick, R.; Schneider, G. A.; Greving, I.; Zierold, R.; Janßen, R. Photonic Materials for High-Temperature Applications: Synthesis and Characterization by X-Ray Ptychographic Tomography. *Appl. Mater. Today* **2018**, *13*, 359–369.

(40) Shabalin, A. G.; Meijer, J.-M.; Dronyak, R.; Yefanov, O. M.; Singer, A; Kurta, § R P; Lorenz, U; Gorobtsov, O. Y.; Dzhigaev, D.; Kalbfleisch, S.; Gulden, J.; Zozulya, A. V; Sprung, M.; Petukhov, A. V; Vartanyants, I. A. Revealing Three-Dimensional Structure of an Individual Colloidal Crystal Grain by Coherent X-Ray Diffractive Imaging. *Physical review letters* **2016**, 117, no. 13, 138002.

(41) Wang, J.; Ahl, S.; Li, Q.; Kreiter, M.; Neumann, T.; Burkert, K.; Knoll, W.; Jonas, U. Structural and Optical Characterization of 3D Binary Colloidal Crystal and Inverse Opal Films Prepared by Direct Co-Deposition. *J. Mater. Chem.* **2008**, *18* (9), 981–988.

(42) Bareigts, G.; Kiatkirakajorn, P.-C.; Li, J.; Botet, R.; Sztucki, M.; Cabane, B.; Goehring, L.; Labbez, C. Packing Polydisperse Colloids into Crystals: When Charge-Dispersity Matters. *Phys. Rev. Lett.* **2020**, *124*.

(43) Pusey, P. N.; Van Megen, W. Phase Behaviour of Concentrated Suspensions of Nearly Hard Colloidal Spheres. *Nature* **1986**, *320* (6060), 340–342.

(44) Meijer, J. M.; Hagemans, F.; Rossi, L.; Byelov, D. V.; Castillo, S. I. R.; Snigirev, A.; Snigireva, I.; Philipse, A. P.; Petukhov, A. V. Self-Assembly of Colloidal Cubes via Vertical Deposition. *Langmuir* **2012**, *28* (20), 7631–7638.

(45) Macfarlane, R. J.; Lee, B.; Jones, M. R.; Harris, N.; Schatz, G. C.; Mirkin, C. A. Nanoparticle Superlattice Engineering with DNA.

(46) Korgel, B. A.; Fullam, S.; Connolly, S.; Fitzmaurice, D. Assembly and Self-Organization of Silver Nanocrystal Superlattices: Ordered "Soft Spheres." *The Journal of Physical Chemistry B* **1998,** 102, no. 43, 8379-8388.

(47) Lokteva, I.; Koof, M.; Walther, M.; Grü, G.; Lehmkü Hler †, F. Coexistence of Hcp and Bct Phases during In Situ Superlattice Assembly from Faceted Colloidal Nanocrystals. *J. Phys. Chem. Lett* **2019**, *10*.

(48) Weidman, M. C.; Yager, K. G.; Tisdale, W. A. Interparticle Spacing and Structural Ordering in Superlattice PbS Nanocrystal Solids Undergoing Ligand Exchange. *Chemistry of Materials,* **2015**, 27, 474-482.

(49) Corricelli, M.; Altamura, D.; Curri, M. L.; Sibillano, T.; Siliqi, D.; Mazzone, A.; Depalo, N.; Fanizza, E.; Zanchet, D.; Giannini, C.;

Striccoli, M. GISAXS and GIWAXS Study on Self-Assembling Processes of Nanoparticle Based Superlattices. *CrystEngComm* **2014**, *16* (40), 9482–9492.

(50) Kuhlmann, M.; Feldkamp, J. M.; Patommel, J.; Roth, S. V.; Timmann, A.; Gehrke, R.; Müller-Buschbaum, P.; Schroer, C. G. Grazing Incidence Small-Angle X-Ray Scattering Microtomography Demonstrated on a Self-Ordered Dried Drop of Nanoparticles. *Langmuir* **2009**, *25* (13), 7241–7243.

(51) Thijssen, J. H. J.; Petukhov, A. V.; 'T Hart, D. C.; Imhof, A.; Van Der Werf, C. H. M.; Schropp, R. E. I.; Van Blaaderen, A. Characterization of Photonic Colloidal Single Crystals by Microradian X-Ray Diffraction. *Adv. Mater.* **2006**, *18* (13), 1662–1666.

(52) Reus, V.; Belloni, L.; Zemb, T.; Lutterbach, N.; Versmold, H. Fusion of Colloidal Crystals Induced by Monovalent and Asymmetric Salt: An Osmotic Pressure and Ultra-Small-Angle X-Ray Scattering Study. *Colloids Surfaces A Physicochem. Eng. Asp.* **1999**, *151* (3), 449–460.

(53) Abramova, V. V.; Sinitskii, A. S.; Grigor'Eva, N. A.; Grigor'Ev, S. V.; Belov, D. V.; Petukhov, A. V.; Mistonov, A. A.; Vasil'Eva, A. V.; Tret'Yakov, Y. D. Ultrasmall-Angle X-Ray Scattering Analysis of Photonic Crystal Structure. *J. Exp. Theor. Phys. 2009 1091* **2009**, *109* (1), 29–34.

(54) Matsuoka, H.; Harada, T.; Yamaoka, H. An Exact Evaluation of Salt Concentration Dependence of Interparticle Distance in Colloidal Crystals by Ultra-Small-Angle X-Ray Scattering. *Langmuir* **2002**, *10* (12), 4423–4425.

(55) Harada, T.; Matsuoka, H.; Ikeda, T.; Yamaoka, H. The Mystery of Colloidal Crystal Formation — Novel Aspects Obtained by Ultra-Small-Angle X-Ray Scattering. *Colloids Surfaces A Physicochem. Eng. Asp.* **2000**, *174* (1–2), 79–98.

(56) Li, T.; Senesi, A. J.; Lee, B. Small Angle X-Ray Scattering for Nanoparticle Research. *Chemical Reviews*. American Chemical Society September 28, 2016, pp 11128–11180.

(57) Okubo, T. Melting Temperature of Colloidal Crystals of Monodisperse Silica Spheres. *The Journal of chemical physics* **1992**, 96, no. 3, 2261-2268.

(58) Okubo, T.; Okada, S.; Tsuchida, A. Kinetic Study on the Colloidal Crystallization of Silica Spheres in the Highly Diluted and Exhaustively Deionized Suspensions as Studied by Light-Scattering and Reflection Spectroscopy. *J. Colloid Interface Sci.* **1997**, *189*, 337–347.

(59) Verhaegh, N. A. M.; Van Duijneveldt, J. S.; Van Blaaderen, A. Direct Observation of Stacking Disorder in a Colloidal Crystal *J. Chem. Phys* **1995**, *102*, 1416.

(60) Schaefer, D. W.; Martin, J. E.; Wiltzius, P.; Cannell, D. S. PHYSICAL REVIEW LETTERS Fractal Geometry of Colloidal Aggregates. **1984**, *52*, 26.

(61) Jiang, P.; Bertone, J. F.; Hwang, K. S.; Colvin, V. L. Single-Crystal Colloidal Multilayers of Controlled Thickness. *Chemistry of Materials,* **1999**, 11, no. 8, 2132-2140.

(62) Russell, J. L.; Tran, N.-L. L.; Mallouk, T. E. Adaptive Shape Ripening and Interparticle Bridging of L-Arginine-Stabilized Silica Nanoparticles during Evaporative Colloidal Crystal Assembly. *ACS applied materials & interfaces,* **2019,** 11, no. 4, 4568-4577.

(63) Yokoi, T.; Sakamoto, Y.; Terasaki, O.; Kubota, Y.; Okubo, T.; Tatsumi, T. Periodic Arrangement of Silica Nanospheres Assisted by Amino Acids. *J. Am. Chem. Soc.* **2006**, *128* (42), 13664–13665.

(64) Míguez, H.; Meseguer, F.; López, C.; Mifsud, A.; Moya, J. S.; Vázquez, L. Evidence of FCC Crystallization of SiO2 Nanospheres. *Langmuir* **1997**, *13* (23), 6009–6011.

(65) Davis, K. E.; Russel, W. B.; Glantschnig, W. J. Settling Suspensions of Colloidal Silica: Observations and X-Ray Measurements. *J. Chem. Soc. Faraday Trans.* **1991**, *87* (3), 411–424.

(66) Miguez, H.; Meseguer, F.; Lopez, C.; Holgado, M.; Andreasen, G.; Mifsud, A.; Fornes, V. Germanium FCC Structure from a Colloidal Crystal Template. *Langmuir* **2000**, *16* (10), 4405–4408.

(67) Hoogenboom, J. P.; Derks, D.; Vergeer, P.; Van Blaaderen, A. Stacking Faults in Colloidal Crystals Grown by Sedimentation. *J. Chem. Phys.* **2002**, *117* (24), 11320.

(68) Russell, J. L.; Noel, G. H.; Warren, J. M.; Tran, N.-L. L.; Mallouk, T. E. Binary Colloidal Crystal Films Grown by Vertical Evaporation of Silica Nanoparticle Suspensions. *Langmuir* **2017**, *33*, 10366–10373.

(69) Marcus, A. H.; Rice, S. A. Observations of First-Order Liquid-to-Hexatic and Hexatic-to-Solid Phase Transitions in a Confined Colloid Suspension. *Phys. Rev. Lett.* **1996**, *77* (12), 2577.

(70) Weidman, M. C.; Smilgies, D.-M.; Tisdale, W. A. Kinetics of the Self-Assembly of Nanocrystal Superlattices Measured by Real-Time in Situ X-Ray Scattering. *Nat. Mater. 2016 157* **2016**, *15* (7), 775–781.

(71) Korgel, B. A.; Fitzmaurice, D. Small-Angle x-Ray-Scattering Study of Silver-Nanocrystal Disorder-Order Phase Transitions. *Phys. Rev. B - Condens. Matter Mater. Phys.* **1999**, *59* (22), 14191–14201.

(72) Park, J.; Zheng, H.; Lee, W. C.; Geissler, P. L.; Rabani, E.; Alivisatos, A. P. Direct Observation of Nanoparticle Superlattice Formation by Using Liquid Cell Transmission Electron Microscopy. *ACS Nano* **2012**, *6* (3), 2078–2085.

(73) Smith, D. K.; Goodfellow, B.; Smilgies, D.-M.; Korgel, B. A. Self-Assembled Simple Hexagonal AB2 Binary Nanocrystal Superlattices: SEM, GISAXS, and Defects. *J. Am. Chem. Soc.* **2009**, *131* (9), 3281–3290.

(74) Goodfellow, B. W.; Yu, Y.; Bosoy, C. A.; Smilgies, D. M.; Korgel, B. A. The Role of Ligand Packing Frustration in Body-Centered Cubic (Bcc) Superlattices of Colloidal Nanocrystals. *J. Phys. Chem. Lett.* **2015**, *6* (13), 2406–2412.

(75) Ackerson, B. J.; Clark, N. A. Shear-Induced Partial Translational Ordering of a Colloidal Solid. *Phys. Rev. A* **1984**, *30* (2), 906.

(76) Krerner, K.; Robbins, M. O. ; Grest, G. S. *Phase Diagram of Yukawa Systems: Model for Charge-Stabilized Colloids*. *Physical review letters,* **1986**, 57, no. 21, 2694.

(77) Monovoukas, Y.; Gast, A. P. The Experimental Phase Diagram of Charged Colloidal Suspensions. *J. Colloid Interface Sci.* **1989**, *128* (2), 533–548.

(78) Cabane, B., Li, J., Artzner, F., Botet, R., Labbez, C., Bareigts, G., Sztucki, M. and Goehring, L."Hiding in plain view: colloidal self-assembly from polydisperse populations." *Physical review letters* 116, **2016**, 20, 208001.

(79) Botet, R.; Cabane, B.; Goehring, L.; Li, J.; Artzner, F. How Do Polydisperse Repulsive Colloids Crystallize? *Faraday Discuss.* **2016**, *186* (0), 229–240.

(80) Bang, J.; Lodge, T.P., Mechanisms and Epitaxial Relationships between Close-Packed and BCC Lattices in Block Copolymer Solutions. *J. Phys. Chem. B* **2003**, *107* (44), 12071–12081.

(81) Moon Jeong Park,; Joona Bang,; Tamotsu Harada, ; Kookheon Char, and; Timothy P. Lodge. Epitaxial Transitions among FCC, HCP, BCC, and Cylinder Phases in a Block Copolymer Solution. *Macromolecules* **2004**, *37* (24), 9064–9075.

(82) Ackerson, B. J.; Hayter, J. B.; Clark, N. A.; Cotter, L. Neutron Scattering from Charge Stabilized Suspensions Undergoing Shear ARTICLES YOU MAY BE INTERESTED IN Neutron Scattering from Charge Stabilized Suspensions Undergoing Shear. *J. Chem. Phys* **1986**, *84*, 2344.

(83) Weidman, M. C.; Nguyen, Q.; Smilgies, D. M.; Tisdale, W. A. Impact of Size Dispersity, Ligand Coverage, and Ligand Length on the Structure of PbS Nanocrystal Superlattices. *Chem. Mater.* **2018**, *30* (3), 807–816.

(84) Gasser, Urs. "Crystallization in three-and two-dimensional colloidal suspensions." *Journal of Physics: Condensed Matter,* **2009**, 21, no. 20, 203101.

(85) Yu, S.-Y.; Cheng, H. Y.; Dysart, J. L.; Huang, Z.; Wang, K.; Mallouk, T. E.; Crespi, V. H.; Badding, J. V.; Mohney, S. E. Scanning Transmission Electron Tomography and Electron Energy Loss Spectroscopy of Silicon Metalattices. Sept 2, **2020**, *arXiv preprint arXiv:2009.01111*.

(86) Russell, J. L.; Tran, N. L. L.; Mallouk, T. E. Adaptive Shape Ripening and Interparticle Bridging of L-Arginine-Stabilized Silica Nanoparticles during Evaporative Colloidal Crystal Assembly. *ACS Appl. Mater. Interfaces* **2019**, *11* (4), 4568–4577.

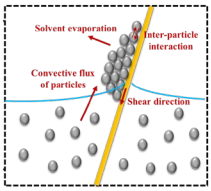

Vertical deposition of
silica nanoparticles
20-125 nm

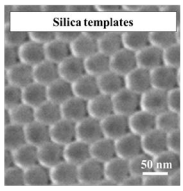

Size based variation
Particle < 31 nm – bcc
> 31 nm – rhcp + 2D hexatic

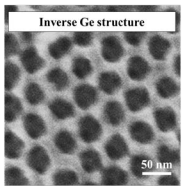

Infiltration in template
using HPCVD
Inherits template structure